Elementary growth mechanisms of creep cavities in AZ31 alloy revealed by in situ X-ray nano-tomography

R. Kumar, P. Lhuissier, J. Villanova, L. Salvo, J.J. Blandin

Elementary growth mechanisms of creep cavities in AZ31 alloy revealed by *in situ* X-ray ~~nanotomography~~

R. Kumar[1,2], P. Lhuissier[2], J. Villanova[1], L. Salvo[2] and J.-.J Blandin[2]

[1] ESRF - The European Synchrotron, CS 40220, 38043 Grenoble Cedex 9, France
[2] University Grenoble Alpes, CNRS, SIMaP, F-38000 Grenoble, France

Corresponding author: Richi Kumar

Abstract

To gain new insights into damage evolution during superplastic deformation, creep cavity growth in commercial Mg alloy (AZ31) was investigated by the novel technique of *in situ* X-ray ~~nanotomography~~. For this, a sample was subjected to deformation under tensile creep conditions (3.2 MPa and 673 K resulting in a strain rate of about 6.6 X10^{-5} s^{-1}) and simultaneously characterized by *in situ* 3D imaging at a pixel size of 100 nm thanks to a scan time of 7 seconds. The sample showed presence of several pre-existing cavities in its initial state (average equivalent radius of less than 1 µm). Evolution of 30 of these cavities was tracked during deformation and it was observed that the cavities followed intricate and unique growth routes, resulting in very complex cavity shapes. An original shape based classification of evolution of cavities was proposed. As a result five evolution types emerged and it was seen that one cavity generally grew by a combination of several evolution types. Individual evolution types were further linked to plausible growth mechanisms and compared with appropriate models. This indicated a combination of diffusion and grain boundary sliding to be the primary growth mechanism responsible for creep cavity growth in the tested condition. It is worth noting that in addition to the expected cavity growth, a reduction in volume of several cavities was also observed during deformation.

Keywords: *In situ*; Grain boundary sliding; Cavity growth; AZ31 alloy; X-ray nano-tomography

1 Introduction

Interest in light alloys has been long driven by the need to lighten structures, on account of reducing greenhouse emissions [1]. While the benefits of usage of light alloys are obvious, room temperature metal forming for such alloys is not the easiest. Hence, hot and warm metal forming are commonly employed to process and shape such alloys [2]. In addition, many aluminum and magnesium alloys have also been known to show superplastic deformation when deformed under specific (generally high) temperature and strain rate. Industrialization of such capabilities for viable metal forming processes, has been keenly pursued over the past few decades. This is especially true for commercial magnesium based alloys, owing to their poor deformability at room temperature [3].

Damage via nucleation and growth of voids or cavities is likely to happen when a material is subjected to high temperature and stresses during plastic or superplastic metal forming or in-service creep conditions. To understand such damage several studies explaining the mechanisms underlying nucleation and growth of cavities have been reported over the decades [4-7]. Such studies have mainly linked the nucleation of cavities to stress concentrations at second phase particles, grain boundaries, and triple junctions [4,7], and attributed the growth of cavities to diffusion, plasticity or superplasticity based mechanisms [4–6]. In addition to theoretical understanding, it is also important to obtain explicit experimental data of such damage to enable comparison with theoretical micromechanical models and advanced numerical simulation. This in turn will also enable accurate damage and failure predictions. However so far most of such studies have been theoretical or conducted using 2D characterization techniques. This is especially true for mechanisms operating during

early stages of cavity growth, which require imaging at high resolution (less than 1 μm). They have mainly been investigated by post mortem techniques like electron microscopy [8]. However, 2D post mortem studies unlike the ones performed *in situ*, do not allow comprehensive analysis of the dynamics of cavity nucleation and growth or the study of very complex shapes as is often the case during superplastic deformation. Over the past few years, *in situ* investigations of creep or high temperature deformation cavities have mainly been carried out using X-ray ~~microtomography~~ [9–13]. However, owing to its limited resolution (coarser than 2 μm), studies have been limited to investigating the late stages of cavity growth driven by plasticity and cavity coalescence. Recently, one study pushed the existing barriers to perform *in situ* 3D imaging at nano scale (pixel size 100 nm) in Al-Cu alloy, to provide new insights into the nucleation and early stages of creep cavity growth driven by diffusion and plasticity [14]. In the present study, the same technique has been used to explore cavity nucleation and growth during deformation of AZ31 alloy in superplastic regime at the nanoscale. An original shape based classification of cavity growth has been proposed and linked to several possible growth mechanisms: plasticity, diffusion, grain boundary sliding.

2 Materials and methods

2.1 Sample preparation

A hot rolled AZ31 alloy sheet of 2 mm thickness was procured from Satzgitter Magnesium-Technologie GmbH. Its composition was 3 wt% of Al, 1 wt% of Zn and 0.4 wt% of Mn. A 10 mm long cylindrical rod with 0.9 mm diameter was machined out of the sheet, such that the cylindrical axis was along the rolling direction of the sheet. In

this rod, a notch of radius 0.2 mm and a minimum cross section diameter of 0.4 mm was machined using a lathe (see Figure 1 a), for *in situ* 3D imaging during creep deformation. A piece of alumina tube, 3 mm in diameter and 2 mm high, was glued on top of the sample to make it compatible with the compact mechanical device. The machining was done such that the tensile direction for creep deformation was parallel to the rolling direction of the sheet. The average grain size measured was 12 μm with a standard deviation of 4 μm. More information about the material, microstructure and its high temperature deformation behavior can be found in [15–18].

2.2 *In situ* ~~nanotomography~~ acquisition of creep deformation

For the experiment, a constant tensile load was applied to the sample at high temperature, while the sample was simultaneously imaged using X-Ray single-distance, phase contrast ~~nanotomography.~~ The setup was such that the sample underwent uninterrupted straining during the test.

In situ X-ray ~~nanotomography~~ [19] was performed at the ID16B [20] insertion device based long, nano-analysis beamline of the European Synchrotron (ESRF). Conic, pink X-ray beam ($\Delta E/E$ nearly 10^{-2}) of 17.5 keV energy was used for imaging. More details about the beamline, furnace and mechanical device can be found in this work [14] which employed the same setup as used in this investigation.

The sample was placed inside the mechanical device and pre stressed to a load of 0.7 (±0.2) N. This was then inserted into the furnace at a temperature of 673 K and the sample underwent creep deformation. The measured strain versus time curve and the corresponding evolution of strain rate with time are shown in Figure 1 (b, c) (the strain and strain rate were measured from the 3D volumes using the method described in

section 2.4). This was estimated at the minimum cross-section of the sample assuming a uniaxial stress state. The deformation was stopped after about 230 minutes (corresponding to a strain of 0.9) before the sample failed. The sample strained fairly uniformly throughout the deformation, maintaining a constant strain rate of nearly 6.6 x 10^{-5} s^{-1}. Using the strain rate jump test conducted on this material in [16], at 673 K between strain rates of 6 x 10^{-5} and 3 x 10^{-4}, its strain rate sensitivity value was found to be close to 0.5. At this strain rate sensitivity materials are known to deform superplastically [21]. Therefore, under the applied conditions this sample was also expected to deform in the superplastic regime. Additionally, due to the notched sample geometry, the stress and strain states were expected to vary spatially, these variations have been estimated and discussed later. Digital Volume Correlation (DVC), was used for local strain field estimation (see section 2.4) and Finite Element Method (FEM) was used for stress field calculation. The FEM simulation was performed using COMSOL multiphysics software using creep norton law and boundary conditions representative of the experiments. While the uniaxial strain increased linearly with time (constant local strain rate), the strain rate was not spatially uniform. Stress field was also non uniform but presented a slow varying triaxiality with sample straining. The average triaxiality is a good description of the stress state and its effect on sample deformation by cavity growth has been discussed later.

3D imaging was done at two different resolutions by changing the distance of the sample with respect to the focused beam and detector, see Figure 1 (d1, d2) for reference. The two resolutions served the following purposes:

- Low Resolution (LR) with a field of view of 826 × 826 × 697 μm^3, pixel size of 645 nm to fully image the notch for computing mechanical deformation parameters.

- High Resolution (HR) with a field of view 128 × 128 × 108 μm^3, pixel size of 100 nm to have sufficient resolution to image cavity nucleation and growth.

During the deformation, alternating tomography scans at LR and HR were continuously acquired. Moreover, in order to increase the field of view of sample at high resolution, four consecutive HR volumes, with an overlap of 18 µm were acquired along different heights of the sample by moving the rotation stage along the z axis (see Figure 1 e, the four HR volumes are indicated as HR1, HR2, HR3 and HR4) resulting in a concatenated volume of 128 × 128 × 377 μm^3. For imaging, 721 projections were acquired by rotating the sample by 360° using a fast pco.edge 5.5 detector (with CMOS sensors) equipped with a 34 µm GGG ($Gd_3Ga_5O_{12}$:Eu) scintillator, resulting in an acquisition time of 7 seconds for a full tomography.

2.3 3D reconstruction

A modified Paganin [22] based approach coupled with an iterative algorithm [23,24] was used to retrieve phase information from distance radiographs. A fixed delta over beta of 280 was defined as a constraint input for the algorithm. The radiographs were processed prior to reconstruction to remove ring artefacts [25]. This was followed by reconstruction by filtered back projection algorithm using the PyHST2 software [26].

2.4 Quantification of 3D volumes

Reconstruction of the 8-bit 3D volumes was followed by the segmentation of different phases: intermetallics, cavities and matrix. Segmentation was done using a cut off threshold. In order to estimate the threshold range, iterative intermeans method [27] was applied on a cropped slice containing a sizable portion of the two different phases.

The LR volumes were used for true stress, strain and strain rate estimations. True stress was estimated by measuring the minimum section of the notch of the sample. To estimate the strain and strain rate on the sample, the intermetallics present in the LR volumes were tracked during deformation using an in-house implementation of the DVC technique. More details about this method can be found here [28]. Additionally, the DVC technique was also used for tracking the position of cavities in the HR volume.

In the HR volume, the two primary phases of intermetallics and cavities were segmented to measure their volume using the Analysis3D plugin of *ImageJ*, which is based on the marching cube algorithm [29]. Subsequently, equivalent radius was calculated from those volumes assuming a spherical shape of cavity or intermetallic. All radii referred to in this work are actually equivalent radii. 3D rendering of the segmented volumes for visualization was done using *Avizo*.

3 Results and discussions

3.1 Initial 3D microstructure

Examination of the HR volume at the start of deformation showed a presence of intermetallics and cavities, see Figure 2 (a) (the intermetallics are shown in green and cavities in red). It can be seen that the sample contains an inhomogeneous distribution of intermetallics which are present in a variable size range and are sometimes seen to be aligned and elongated along the rolling direction. In addition to the intermetallics, cavities are also present at the beginning of deformation. Pre-existing cavities have been reported in hot rolled sheets of AZ31 alloys [30], and are attributed to be a by-product of the thermo mechanical treatment undergone by the sheets.

Figure 2 (b1, b2) shows the probability distribution of radius of the intermetallics and pre-existing cavities. It can be seen that the majority of the intermetallics (60%) have a radius of less than 0.5 µm and most of the pre-existing (70%) cavities have radius of less than 1 µm. Similar investigations of *in situ* deformation via X-ray microtomography reported previously [9,10], done with an effective resolution of nearly 2 µm, did not report intermetallics and pre-existing cavities of less than 1 µm because limited resolution makes them blind to small features in this size range. These small cavities would grow upon sample deformation and when they are big enough to be resolved, they would be classified as cavities/voids nucleated during deformation. While current investigation shows that this might not be true. Therefore, *in situ* X-ray ~~nanotomography~~ investigation of deformation of sample clearly allows a more comprehensive information about the initial microstructure of the sample, making further analysis more accurate.

3.2 First qualitative analysis of cavity growth

Thanks to high resolution 3D imaging, creep damage in the sample was investigated by following the growth of individual cavities as the sample deformed. A total of 30 cavities were tracked from the last state of deformation to the beginning of deformation. Note that each cavity was given an ID which is consistent throughout the text (Eg. the cavity number 9 referred in Figure 3 a is the same as the one referred in Figure 7). As only a part of the sample is imaged in HR (indicated by ROI Figure 1 e), this region changes with respect to the sample, because of sample deformation. Only cavities that were present in the ROI for several deformation states during the *in situ* test could be tracked. All the remaining cavities have been excluded from the study.

A 3D rendered view of the evolution of three cavities during the deformation has been shown in Figure 3 and Figure 4 (cavities are shown in red and intermetallics in green). They illustrate different patterns of growth that were observed. Visual examination of the growth of cavities showed that the cavities took complex shapes during deformation and were not merely spherical or elliptical in shape. Thanks to the *in situ* 3D imaging at high resolution, the pathway of evolution of cavities into this complex shape could also be visualized. It was noted that at the beginning of deformation, the cavities appeared equiaxed and spherical (at the current resolution), and during deformation they grew and took complex shapes. It was also noted that contrary to expectations, few cavities also showed shrinkage under the applied load. An example of this can be seen in Figure 4 where the cavity is seen to show shrinkage after a strain of 0.74. This reduction in volume of cavity during deformation was unexpected given that the sample was subjected to a tensile load.

In order to understand the growth of cavities during creep deformation and to gain added insights into their growth mechanisms, the observed shape changes were classified for further examination.

3.3 Shape based classification of cavity growth patterns

After studying the change in shapes seen in the cavities during creep deformation, a new approach to classify their growth has been proposed. This approach is based on monitoring the growth of cavities in 3 orthogonal directions. However, owing to the complex growth patterns, defining these orthogonal directions was not straightforward. It was seen that each cavity had a different principal direction of growth, and this often did not correspond to the directions parallel or orthogonal to the tensile axis. Hence,

following the growth of cavities along these standard directions was not enough to understand their growth.

This has been illustrated by a schematic in Figure 5 (a) where a cavity grows from a small, nearly equiaxed shape to an elongated shape on application of tensile load at high temperature. The predominant direction of this growth is neither along, nor orthogonal to the direction of tensile loading. In such a case, measuring the growth of cavity with respect to a standard bounding box shown in blue dotted line in Figure 5 (b1), with principal directions x, y, z; orthogonal (x, y) and parallel (z) to the tensile direction would not be sufficient to illustrate the growth observed. On the other hand, the bounding box shown in Figure 5 (b2) in green, with principal axis l, w, d and lengths of L, W, D is a more appropriate box to follow the shape change. In the second case, it is easier to follow that the predominant growth is in the 'l' direction. Therefore, the shape change of this cavity is better understood by following the change in lengths L, W, D rather than following the change in lengths of X, Y and Z.

Following this idea, a unique local bounding box was defined for each cavity such that the principal directions of this box corresponded to an average principal growth direction observed for that cavity. Because this direction differed for each cavity and even for one cavity it often varied as the cavity grew, it had to be determined manually by observing the growth patterns in 3D.

After carefully analyzing the growth patterns based on evolution of the bounding boxes seen in the tracked cavities, the evolution was classified into five categories. These classifications will be referred to as **evolution types** in this text and refer to the morphology evolution of the cavities, and should not be confused with **growth**

mechanisms like diffusion, grain boundary sliding etc. It should be noted that during the deformation, one cavity evolved by a combination of different evolution types.

The classification of evolution type is the following (illustrated schematically in Figure 6 a-e using montage of cavity growth and corresponding evolution of lengths of bounding boxes in plots on the right side of each type):

- Type 1A evolution is where the growth is equal in all directions such that the volumetric increase is not accompanied by any change in shape of the cavity (see Figure 6 a).
- Type 1B evolution is similar to Type 1A in the sense that the cavity grows multi-directionally. However, the difference lies in the fact that growth is not uniform in all directions (see Figure 6 b). Following variations were observed in this evolution:
    - Growth concentrated in a small portion of the cavity
    - Growth restricted in a certain direction

  Nevertheless, this type of growth resulted in fairly equiaxed but faceted cavities.
- Type 2 corresponds to growth which is considerably accelerated in two dimensions as compared to the third, resulting in a flat or planar cavity (see Figure 6 c).
- Type 3 evolution corresponds to a very specific pattern of growth where growth is highly accelerated in one dimension which does not lie along the axis of tensile loading (see Figure 6 d).
- Type 4 pertains to the case where instead of growth there is a decrease in volume of the cavity. This decrease may or may not involve a change in shape of the cavity (see Figure 6 e).

For each evolution type, a corresponding symbol has been defined below it, in Figure 6 (a-e). This classification is helpful in dissecting the growth montage of cavity 9,26 and 15 shown in Figure 3 and Figure 4, where the relevant evolution type for each stage has been indicated using symbols at top left corner.

As a detailed example, Figure 7 shows the evolution of the lengths of bounding box (L, W and D) of the cavity number 9 (see Figure 3 a for growth montage of this cavity) where the different evolution types have been marked. Here, it can be seen that initially the growth is equal in all dimensions showing Type 1A evolution. Later, after a strain of 0.1, an accelerated growth along the L dimension, which is a signature of Type 3 growth, is seen. After a strain of 0.37, growth picks up along W eventually stopping along L. Since the growth proceeds multi dimensionally (along W and D) at different rates, it has been classified as Type 1B growth.

3.4 Tracking of individual cavity evolution

Figure 8 (a) shows the pathway of evolution for the 30 tracked cavities with respect to time, using the classification shown in the previous section. Absence of data at certain times is due to the fact that for those values, either the corresponding cavity was no longer in the field of view and hence could not tracked or it was too small to be resolved in the images (for example cavities number 17 and 18). Such a map provides an aggregate information of patterns of growth seen in the sample.

Most evidently, Figure 8 confirms the observations already shown for cavity numbers 9, 26 and 15 (in Figure 3 and Figure 4), that one cavity grows by a combination of different evolution types. For example, growth for cavity number 7 starts by type 1A and then changes to Type 3 evolution, after which 1B Type evolution takes over. It can

be seen that for many cavities, the growth initiates with 1A Type (few exception being cavity number 11, 24, 25). Type 1B is the most frequent evolution type and is seen during evolution of nearly all cavities. Type 2 and 3 are less commonly observed (one example of each are cavity number 26 and 28 respectively). Type 4 evolution on the other hand is frequent. It can be seen that most cavities that show shrinkage, are in fact preceded by a phase of volumetric growth (for example cavity numbers 14 and 30). Further, to examine the effect of change in stress and strain owing to sample geometry on cavity evolution Figure 8 (b) shows the same map with respect to the local strain around each cavity, the local stress triaxiality has also been mentioned on the second y axis. It was seen that Type 4 and 2 are seen in cavities with triaxiality above 0.5 and at very low strain values below 0.1 only Type 1A is seen. Apart from this no specific relation between the strain values and stress triaxiality was seen on the evolution types.

3.5 Understanding cavity evolution using growth mechanisms

3.5.1 Theoretical cavity growth models

Cavity growth is known to be driven by several different mechanisms like plasticity, diffusion, superplasticity etc. [4,5]. Different driving forces for growth (like vacancies, matrix plasticity, grain boundary sliding etc.) are likely to result in different shape changes in a growing cavity [31–33]. Before delving into experimental results, the cavity growth mechanisms relevant to current study are briefly presented in this section.

3.5.1.1 Diffusion dominated cavity growth mechanism

Growth by diffusion is known to be driven by the diffusion of excess vacancies. From the pioneering work of studying diffusion based cavity growth by Hull and Rimmer [34] several other modifications to the proposed theory have been made over the years [35–39]. The basic principle is that excess vacancies are created on the grain boundary due to applied tensile stress. These excess vacancies diffuse to the cavities, which provide sinks of low chemical potential, to cause their growth.

For a periodic array of cavities with radius r, separated by a distance $2l$ lying on a grain boundary with a stress of σ acting perpendicular to the grain boundary (Figure 9 a), Raj et al [35,36] proposed volumetric growth of voids will be caused by diffusion of matter from void surface into the grain boundary. The rate of growth affected by lattice diffusion would then be given by:

$$\left(\frac{dV}{dt}\right)_l = \frac{2\Omega D_l(2l)}{kT}\left\{\frac{\left(\sigma - \frac{2\gamma}{r}\right)(1-\omega^2)}{ln\left(\frac{1}{\omega}\right) - 0.75 + \omega^2\left(1 - \frac{\omega^2}{4}\right)}\right\} \quad (1)$$

Where $\omega = r/l$, $2l$ is taken as the grain size for lattice diffusion based growth, other symbols have been defined in Table 1.

In addition to the classical diffusion models, constrained grain boundary growth models have also been proposed which account for the inhomogeneous distribution of cavities in polycrystalline samples. As per Rice [37], growth rate for constrained cavity growth via grain boundary diffusion is given by:

$$\left(\frac{dV}{dt}\right)_{cgb} = \frac{4\pi\Omega\delta D_{gb}}{kT}\left\{\frac{\sigma - (1-\omega^2)\left(\frac{2\gamma\sin(\psi)}{r}\right)}{\frac{4L^3}{\alpha_r l^2(f_s)} + ln\left(\frac{1}{\omega^2}\right) - \frac{(3-\omega^2)(1-\omega^2)}{2}}\right\} \quad (2)$$

where, $L = \left(\frac{\sigma\Omega\delta D_{gb}}{\dot{\varepsilon}kT}\right)^{\frac{1}{3}}$, $2l$ is taken as half of the grain size for grain boundary diffusion based growth and other parameters are mentioned in Table 1

3.5.1.2 Grain boundary sliding controlled cavity growth mechanism

Cavities are also known to grow by grain boundary sliding. For deformation where grain boundary sliding is considerable, the diffusive growth of cavities will be affected by grain boundary sliding. Riedel [40] proposed that cavities on tensile ledges of grain boundaries grow directly under the effect of grain boundary sliding. The kinetics of cavity growth in such situations is driven by the kinetics of boundary sliding. Based on a 2D cavity geometry shown in Figure 9 (b1) lying on a boundary with a grain boundary sliding rate of $\dot{u}_b$, the cavity growth rate is given by:

$$2\frac{dr}{dt} = \dot{u}_b \tag{3}$$

For a 3D geometry, the volumetric growth rate is given by:

$$\frac{dV}{dt} = 2A_c\frac{dr}{dt} = A_c\dot{u}_b \tag{4}$$

where the cavity is represented as a cylinder of length $2r$ and cross-section A_c, which lies on a grain boundary sliding at rate $\dot{u}_b$ (Figure 9 b2). It is assumed that the cross-section transverse to the sliding direction remains constant, and that only the length of the cavity would increase due to sliding.

3.5.2 Comparison of theoretical models with experiments

In this section, shape based classification of each evolution type (except Type 2, due to lack of experimental data and appropriate models) is linked to an appropriate growth mechanism, for the duration that the cavity follows a particular evolution type.

Moreover, for the plausible growth mechanism, theoretical volumetric growth rate has been compared to the measured volumetric growth rate. It is noteworthy that as the cavities grow by a combination of different evolution types, they should in fact also grow by a combination of different growth mechanisms.

3.5.2.1 Type 1A

As shown in Figure 6 (a), shape analysis of Type 1A indicates an isotropic growth since all dimensions grow at the same rate. It is known that growth by diffusion is driven by as an equal influx of vacancies into the cavity from all directions, and is expected to lead to no shape changes in the growing cavity. Hence, Type 1A growth pattern is consistent with growth driven by diffusion.

In Figure 10, the volumetric growth rate measured experimentally for cavity number 8, for the duration that it evolves by Type 1A, is compared to different diffusion growth models. The experimental growth rate dV/dt (red markers) is calculated from the volume of cavity measured at each time step and the cavity radius is estimated from the volume assuming a spherical shape of cavity. The black plot corresponds to the grain boundary diffusion model by Raj and Ashby modified to accommodate lattice diffusion [35,36], (Equation 1 in Section 3.5.1.1). The red plot refers to the constrained grain boundary diffusion model proposed by Rice [37], which predicts the growth rate for constrained cavity growth via grain boundary diffusion (Equation 2 in Section 3.5.1.1).

The value for the relevant parameters of the two equations are mentioned in Table 1. (Data for pure Mg has been considered, where data for AZ31 alloy was unavailable)

Table 1 Parameters used for plotting volumetric growth rate of cavities for different diffusion based models. (Relevant data for pure Mg was considered, where data for AZ31 alloy was unavailable)

Variable	Value	Reference

Ω (m^3): Atomic volume	2.33 x 10^{-28}	
δD_{gb} (m^3s^{-1}) δ : Grain boundary width D_{gb} : Grain boundary diffusivity	5 X 10^{-12}exp(-92000/RT)	[41]
D_l (m^2s^{-1}): Lattice diffusivity	1 X 10^{-4}exp(-135000/RT)	[41]
T (K): Temperature	673	This work
σ (MPa): Stress	3.2	This work
γ (Jm^{-2}): Surface energy	0.78	[42]
$\dot{\varepsilon}$ (s^{-1}): Strain rate	6.6 X 10^{-5}	This work
f_s (m): Facet size	6 X 10^{-6}	This work
d (m): Grain size	12 X 10^{-6}	This work
ψ (°): Angle of cavity on grain boundary	70	[37]
α_r : Dimensionless factor.	0.8	[37]

Both models present a good match with the experimental values. Other cavities growing by this evolution type in most cases also show similar trends. Hence, both shape based changes and comparison with theoretical model support the claim that Type 1A growth could be driven by diffusion. It is worth noting that the classical grain boundary diffusion model [35,36] (not plotted here) predicted growth rates nearly two orders of magnitude higher than the measured growth rates. It is recognized that accurate diffusivity values for grain boundary and lattice diffusion are needed to establish this with certainty.

3.5.2.2 Type 1B and 3

Type 1B and Type 3 are discussed together using the example of a very unique and specific cavity (number 9) that evolved by a combination of both and also showed an indirect signal of grain boundary sliding.

Type 1B evolution involved complex shape changes and was therefore likely to be a result of a combination of several mechanisms. Because there is no discernible

preference to the tensile axis, plasticity mechanism was discarded as a causative driving force for growth. The multidimensional nature of the growth suggested a contribution by diffusion. Considering the experimental conditions, it can be most probably coupled with a directional mechanism like grain boundary sliding.

Type 3 evolution was marked by a unidirectional growth, which implies a non-uniform driving force. Plasticity and grain boundary sliding are two such directional and non-uniform growth mechanisms. Nevertheless, plasticity under uni-axial stress is expected to cause predominant cavity growth along the tensile axis, which is not what was observed for cavities associated with Type 3 evolution. Instead, the observed shape changes closely resembled that predicted by grain boundary sliding based growth [33]. Hence, Type 3 was attributed to be driven by grain boundary sliding.

Cavity number 9 presented in Figure 3 (a) grew by a sequence of 3 different evolution types: (i) Type 1A (strain range: 0-0.07), (ii) Type 3 (strain range: 0.12-0.37) and (iii) Type 1B (strain range: 0.39-0.92). Interestingly, this cavity had a line-up of intermetallics present above and below it. As illustrated in Figure 11 (a1), a close examination of these intermetallics (in green) shows displacement in opposite directions with increasing strain. In Figure 11 (a2), intermetallics at a low strain state (in grey) are superimposed over the same at higher strain state (in green), the cavity (in red) in the higher strain state has also been shown for reference. Examining the position of green intermetallics with respect to grey, it can be seen that the top part is sliding with respect to the bottom part. This can be interpreted as two grains sliding against each other, the cavity being on the grain boundary in between. The orientation of this boundary is unknown, but it should be a plane composing the sliding direction (possible sliding direction has been indicated by a black arrow and plausible plane orientations have also been indicated schematically in Figure 11 a2).

This movement of the intermetallic was measured and used to estimate the experimental grain boundary sliding direction, displacement and rate. Several intermetallics on each side of the grain boundary were chosen and their average displacement vector was computed. It was seen that there were two primary sliding directions (named S1 and S2). Since these sliding directions had to be present on the sliding grain boundary, a cross product of the two gave the normal to the grain boundary plane (named NGB). Figure 11 (a3) shows a schematic representation of the definition of the different vectors.

The net increase of cavity length along S1 and S2 directions were compared to grain boundary displacement in these directions, shown in Figure 11 (b1, b2). It was seen that the net increase in length of the cavity was proportional to the grain boundary displacement in S1 direction until a displacement of nearly 6 μm, which corresponded to a strain of 0.5. After this, the cavity did not grow in S1 but instead, it grew in S2 direction proportional to the grain boundary displacement. This pointed towards a link of the increase in cavity length to the displacement of the sliding boundary. Furthermore, the measured grain boundary displacements were used to estimate the grain boundary sliding rate. The average of grain boundary sliding rate in direction S1 and S2 was found to be nearly the same: 6.5×10^{-10} ms^{-1}.

Using the measured grain boundary sliding rate, a comparison with a grain boundary model for cavity growth has been attempted.

The two parameters needed for this models were: grain boundary sliding and cross section of cavity transverse to sliding direction. For cavity number 9, the local grain boundary sliding rate was measured. Additionally, since the sliding directions were known, the cavity cross-section transverse to the two sliding directions (A1 and A2 transverse to S1 and S2 respectively) were also known. This allowed calculating

theoretical volumetric growth rate with parameters true to local conditions experienced by the cavity. The theoretical volumetric growth rate for the two sliding directions are shown in Figure 12 (a) using red and green lines respectively, indicated by GBS1 and GBS2. They were compared with the experimental volumetric growth rate of the cavity, where magenta markers refer to the duration it evolved by Type 3 while the black markers refer to its Type 1B evolution. A close match of the experimental values to the model is visible. The jump in the experimental growth values with an increase in radius can be attributed to the change in the sliding direction. As the sliding direction changes the cross section transverse to it would also change, and if this cross section is larger, it is expected to lead to an increase in the growth rate.

These observations help in establishing the fact that both Type 3 and Type 1B evolutions involve grain boundary sliding. Here, it should be noted that at larger radius the volumetric growth rate deviates from the model. This could be because of the non-negligible contributions of diffusion to growth of cavity. Absence of appropriate models combining the effect of diffusion and grain boundary sliding make further explanation difficult.

3.5.2.3 Type 4

In this section, the cavities showing Type 4 evolution or a decrease in volume will be examined. It is know that a cavity would shrink if the applied stress on it is less than $\sigma = \frac{2\gamma}{r}$. Figure 12 (b) shows a plot of 2γ/r for all cavities that showed Type 4 evolution, along with the initial applied true stress indicated using a red marker on the same plot. It can be seen that the applied stress is always greater than 2γ/r for all the cavities. Despite this active diffusive sintering of these cavities was observed. One reason for this could be that the stress field inside the sample is complex and uneven resulting in

a much less effective stress on the cavities. And when the net stress on the cavity is less than 2γ/r, it would began to sinter under the effect of high temperature [4].

It is important to note that according to Figure 8, most of the cavities associated with Type 4 initially showed an increase in volume, and then shrank. This indicates that during deformation, the stress experienced by the cavities changed. Perpetual grain boundary sliding in the sample could give rise to such changing stress states in the sample. A complex and evolving stress state in polycrystalline materials showing prominent grain boundary sliding has in fact been reported [15].

4 Conclusions

Tensile creep deformation of AZ31 alloy sample and the accompanied creep cavity growth was characterized using the novel technique of *in situ* X- ray ~~nanotomography.~~ The high resolution imaging of sample before deformation showed the presence of several pre-existing cavities of radius smaller than 1 μm, which cannot be resolved by conventional microtomography characterization. The growth of 30 such cavities were tracked during deformation and following observation were made:

- Cavities followed intricate and unique growth patterns which resulted in complex shapes during deformation.
- To dissect this growth, shape based classification of cavity growth was done into 5 categories: called evolution types. It was seen that one cavity generally grew by a combination of several evolution types.
- Individual evolution types were linked to plausible growth mechanisms and then compared to appropriate models. A combination of diffusion and grain boundary sliding was found to be the primary growth mechanism responsible for creep

cavity growth. It was acknowledged that a more robust model that accounted for a combined effect of grain boundary sliding and diffusion was needed to explain the growth of cavities more conclusively.

- In a very specific case, an indirect evidence for grain boundary sliding was spotted near a cavity thanks to the observed motion of intermetallics in opposite directions, and the following observations were made:
    - A change in sliding direction was seen for the set of grains during deformation.
    - The grain boundary displacement was found proportional to the increase in cavity length in the sliding directions, indicating sliding driven growth.
    - The grain boundary sliding rate was measured in 3D and used in grain boundary sliding driven cavity growth model. The model predicted volumetric growth rates very close to the measured values for the specific cavity, further showing grain boundary driven growth.
- In addition to growth, a very unconventional phenomenon was observed where several cavities showed a decrease in volume during deformation. This was attributed to sintering of cavities via diffusion due to reduced local stress.

5 Acknowledgment

The authors acknowledge the efforts of Xavier Bataillon and Charles Josserond, technical staff at SIMaP laboratory, University Grenoble Alpes, Sylvain Laboure, technician at ID16B, ESRF and Cyril Guilloud, Pierre Paleo and Henri Payno, engineers at ESRF. And we are grateful to ESRF and Labex CEMAM for the PhD grant and allocated beamtime for proposal number MA3507.

6 Bibliography

[1] Z. Yang, J.P. Li, J.X. Zhang, G.W. Lorimer, J. Robson, Review on Research and Development of Magnesium Alloys, Acta Metall. Sin. (English Lett. 21 (2008) 313–328. https://doi.org/10.1016/S1006-7191(08)60054-X.

[2] G.S. Cole, A.M. Sherman, Light weight materials for automotive applications, Mater. Charact. 35 (1995) 3–9. https://doi.org/10.1016/1044-5803(95)00063-1.

[3] R. Boissière, J.J. Blandin, L. Salvo, Large Deformability of Wrought Magnesium Alloys: Is Superplasticity Needed?, Key Eng. Mater. 433 (2012) 267–272. https://doi.org/10.4028/www.scientific.net/kem.433.267.

[4] M.E. Kassner, T.A. Hayes, Creep cavitation in metals, Int. J. Plast. 19 (2003) 1715–1748. https://doi.org/10.1016/S0749-6419(02)00111-0.

[5] A.J. Perry, Cavitation in creep, J. Mater. Sci. 9 (1974) 1016–1039. https://doi.org/10.1007/BF00570398.

[6] A. Pyzalla, B. Camin, T. Buslaps, M. Di Michiel, H. Kaminski, A. Kottar, A. Pernack, W. Reimers, Simultaneous tomography and diffraction analysis of creep damage, Science (80-.). 308 (2005) 92–95. https://doi.org/10.1126/science.1106778.

[7] R. Raj, Nucleation of cavities at second phase particles in grain boundaries, Acta Metall. 26 (1978) 995–1006. https://doi.org/10.1016/0001-6160(78)90050-0.

[8] J. He, R. Sandström, Creep cavity growth models for austenitic stainless steels, Mater. Sci. Eng. A. 674 (2016) 328–334. https://doi.org/10.1016/j.msea.2016.08.005.

[9] H. Toda, Z. Azri, B. Shamsudin, K. Shimizu, K. Uesugi, Cavitation during high-temperature deformation in Al – Mg alloys, Acta Mater. 61 (2013) 2403–2413. https://doi.org/10.1016/j.actamat.2013.01.012.

[10] P. Lhuissier, M. Scheel, L. Salvo, M. Di Michiel, J.J. Blandin, Continuous characterization by X-ray microtomography of damage during high-temperature deformation of magnesium alloy, Scr. Mater. 69 (2013) 85–88. https://doi.org/10.1016/j.scriptamat.2013.03.001.

[11] H.M.M.A. Rashed, J.D. Robson, P.S. Bate, B. Davis, Application of X-ray microtomography to analysis of cavitation in AZ61 magnesium alloy during hot deformation, Mater. Sci. Eng. A. 528 (2011) 2610–2619. https://doi.org/10.1016/j.msea.2010.11.083.

[12] A. Isaac, F. Sket, W. Reimers, B. Camin, G. Sauthoff, A.R. Pyzalla, In situ 3D quantification of the evolution of creep cavity size, shape, and spatial orientation using synchrotron X-ray tomography, Mater. Sci. Eng. A. 478 (2008) 108–118. https://doi.org/10.1016/j.msea.2007.05.108.

[13] K. Dzieciol, A. Borbély, F. Sket, A. Isaac, M. Di Michiel, P. Cloetens, T. Buslaps, A.R. Pyzalla, Void growth in copper during high-temperature power-law creep, Acta Mater. 59 (2011) 671–677. https://doi.org/10.1016/j.actamat.2010.10.003.

[14] R. Kumar, J. Villanova, P. Lhuissier, L. Salvo, In situ nanotomography study of creep cavities in Al-3.6-Cu alloy, Acta Mater. 166 (2019) 18–27. https://doi.org/10.1016/j.actamat.2018.12.020.

[15] T. Dessolier, Effet de la température sur les hétérogénéités de déformation plastique dans les alliages de magnésium Effect of the temperature on the heterogeneites of deformation in magnesium alloys, UNIVERSITE GRENOBLE

ALPES, 2018.

[16] R. Boissiere, Effect de la temperature sur les capacites de mise en forme d'alliages de magnesium corroyes, Institute polytechnique de grenoble, 2008.

[17] T. Dessolier, G. Martin, P. Lhuissier, C. Josserond, F. Roussel, F. Charlot, J.-J. Blandin, L. Maniguet, Conducting Controlled In Situ High Temperature Tensile Tests within a SEM, Microsc. Anal. (2018). https://microscopy-analysis.com/article/july_18/High_Temperature_Tensile_Testing_in_situ.

[18] T. Dessolier, P. Lhuissier, F. Roussel-Dherbey, F. Charlot, C. Josserond, J.-J. Blandin, G. Martin, Effect of temperature on deformation mechanisms of AZ31 Mg-alloy under tensile loading, Mater. Sci. Eng. A. 775 (2020) 138957. https://doi.org/https://doi.org/10.1016/j.msea.2020.138957.

[19] J. Villanova, R. Kumar, R. Daudin, P. Lhuissier, D. Jauffrès, L. Christophe, R. Tucoulou, S. Labouré, G. Martinez-criado, L. Salvo, Fast In Situ Nanotomography at ESRF, Microsc. Microanal. 24 (2018) 450–451. https://doi.org/10.1017/S1431927618014496.

[20] G. Martinez-Criado, J. Villanova, R. Tucoulou, D. Salomon, J.P. Suuronen, S. Laboure, C. Guilloud, V. Valls, R. Barrett, E. Gagliardini, Y. Dabin, R. Baker, S. Bohic, C. Cohen, J. Morse, ID16B: A hard X-ray nanoprobe beamline at the ESRF for nano-analysis, J. Synchrotron Radiat. 23 (2016) 344–352. https://doi.org/10.1107/S1600577515019839.

[21] T.G. Langdon, The physics of superplastic deformation, Mater. Sci. Eng. A. 137 (1991) 1–11. https://doi.org/10.1016/0921-5093(91)90312-B.

[22] D. Paganin, Coherent X-Ray Optics, Oxford University Press, Oxford, 2006.

[23] M. Langer, A. Pacureanu, H. Suhonen, Q. Grimal, P. Cloetens, F. Peyrin, X-Ray Phase Nanotomography Resolves the 3D Human Bone Ultrastructure, PLoS One. 7 (2012) 1–7. https://doi.org/10.1371/journal.pone.0035691.

[24] L. Weber, Iterative tomographic X-Ray phase reconstruction, 2016. http://theses.insa-lyon.fr/publication/2016LYSEI085/these.pdf.

[25] B. Münch, P. Trtik, F. Marone, M. Stampanoni, Stripe and ring artifact removal with combined wavelet-Fourier filtering, EMPA Act. 17 (2009) 34–35. https://doi.org/10.1364/OE.17.008567.

[26] A. Mirone, E. Brun, E. Gouillart, P. Tafforeau, J. Kieffer, The PyHST2 hybrid distributed code for high speed tomographic reconstruction with iterative reconstruction and a priori knowledge capabilities, Nucl. Instruments Methods Phys. Res. Sect. B Beam Interact. with Mater. Atoms. 324 (2014) 41–48. https://doi.org/10.1016/j.nimb.2013.09.030.

[27] T.W. Ridler, S. Calvard, Picture Thresholding Using an Iterative Selection Method, IEEE Trans. Syst. Man Cybern. 8 (1978) 630–632. https://doi.org/10.1109/TSMC.1978.4310039.

[28] L. Lhuissier, Pierre , Bormann, Therese, Pelloux, Guillaume , Bataillon, Xavier , Pelloux, Franck , Josserond, Charles , Gravier , Pauline , Blandin, Jean-Jacques , Boller, Elodie , Salvo, High-temperature deformation followed in situ by X-ray microtomography: a methodology to track features under large strain, J. Synchrotron Radiat. (2021).

[29] V. Boulos, V. Fristot, D. Houzet, L. Salvo, P. Lhuissier, Investigating performance variations of an optimized GPU-ported granulometry algorithm, in: 18th Int. Eur. Conf. Parallel Distrib. Comput., 2012.

[30] R. Boissière, J.J. Blandin, L. Salvo, Damage Development During Superplasticity of Light Alloys, J. Eng. Mater. Technol. 130 (2008) 021014. https://doi.org/10.1115/1.2884335.

[31] X.G. Jiang, J.C. Earthman, F.A. Mohamed, Cavitation and cavity-induced fracture during superplastic deformation, J. Mater. Sci. 29 (1994) 5499–5514. https://doi.org/10.1007/BF00349941.

[32] J. Hancock, Creep cavitation without a vacancy flux, Met. Sci. 10 (1976) 319–325. https://doi.org/10.1179/msc.1976.10.9.319.

[33] I.W. Chen, Cavity growth on a sliding grain boundary, Metall. Trans. A. 14 (1983) 2289–2293. https://doi.org/10.1007/BF02663303.

[34] D. Hull, D.E. Rimmer, The growth of grain- boundary voids under stress, Philos. Mag. 4 (1959) 673–687. https://doi.org/10.1080/14786435908243264.

[35] R. Raj, M.F. Ashby, Intergranular fracture at elevated temperature, Acta Metall. 23 (1975) 653–666. https://doi.org/10.1016/0001-6160(75)90047-4.

[36] R. Raj, H.M. Shih, H.H. Johnson, CORRECTION TO: INTERGRANULAR FRACTURE AT ELEVATED TEMPERATURE, Scr. Metall. 11 (1977) 839–842.

[37] J.R. Rice, Constraints on the diffusive cavitation of isolated grain boundary facets in creeping polycrystals, Acta Metall. 29 (1980) 675–681.

[38] W. Beere, M. Speight, Creep cavitation by vacancy diffusion in plastically deforming solid, Met. Sci. 12 (1978) 172–176. https://doi.org/10.1179/msc.1978.12.4.172.

[39] B.F. Dyson, Constraints on diffusional cavity growth rates, Met. Sci. 10 (1976) 349–353. https://doi.org/10.1179/030634576790431417.

[40] H. Riedel, Fracture of high temperature, 1st ed., Springer-Verlag Berlin Heidelberg, 1987. https://doi.org/10.1007/978-3-642-82961-1.

[41] H.J. Frost, M.F. Ashby, Deformation-mechanism Maps: The Plasticity and Creep of Metals and Ceramic, 1982.

[42] L. Vitos, A.V. Ruban, H.L. Skriver, J. Kollar, The surface energy of metals, Surf. Sci. 411 (1988) 186–202. https://doi.org/10.1016/S0039-6028(98)00363-.

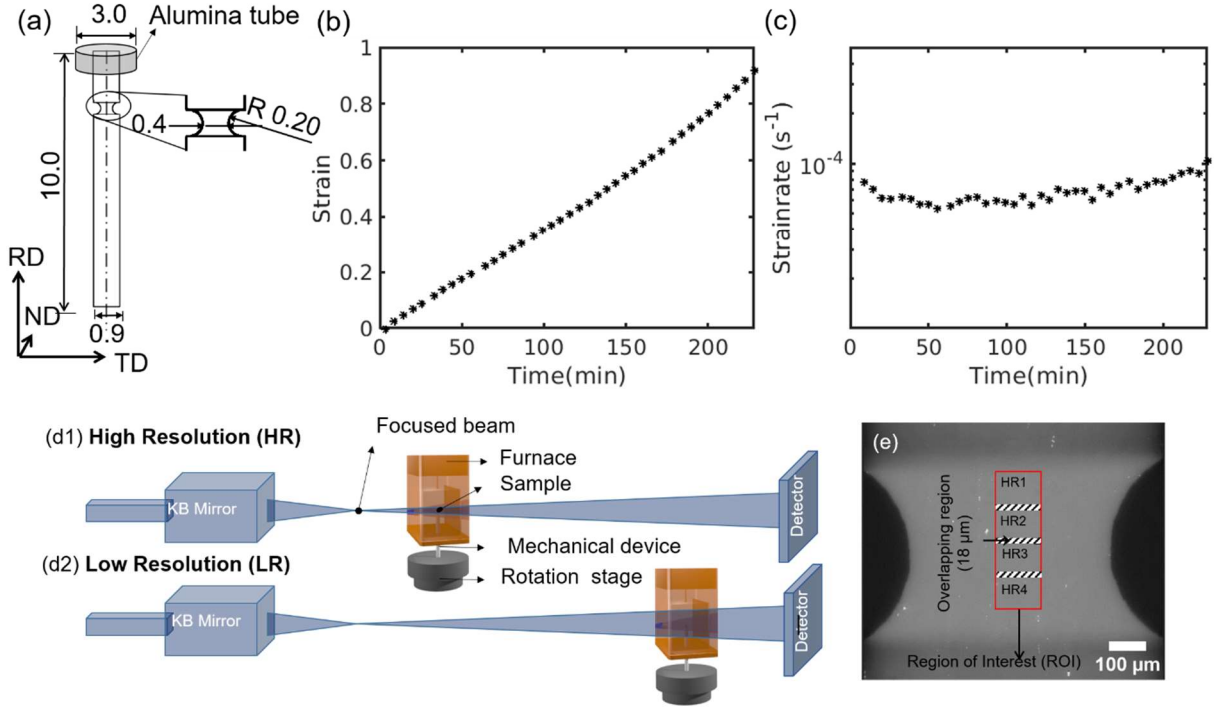

Figure 1 (a) Drawing of the sample investigated (all measurements in mm RD: Rolling direction ND: Normal to rolling direction and TD: Transverse to rolling direction), with a magnified view of the notch. Plots showing evolution of (b) strain and (c) strain rate with time. (d1-d2) Schematic illustration of positions of furnace and sample with respect to the focused beam at (d1) High Resolution (pixel size is 100 nm) and (d2) Low Resolution (pixel size is 645 nm). (e) A transverse 2D slice from LR volume depicting the scheme of acquisition where 4 HR volumes are acquired as indicated by HR1 to HR4. The overlap between successive HR scans is of 18 µm and is shown as shaded region. ***Intended for color reproduction on the web version.***

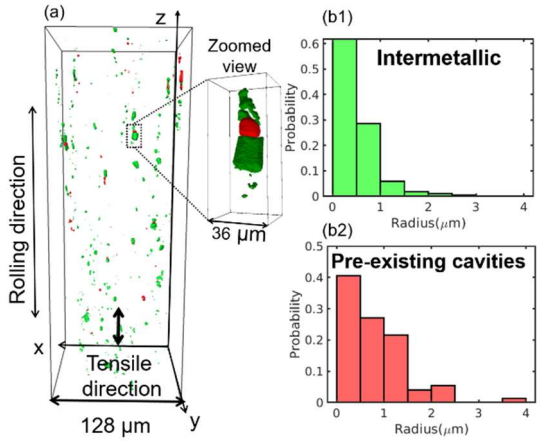

Figure 2 (a) 3D HR rendered volume (pixel size 100 nm) of sample at the start of deformation (intermetallics in green and cavities in red). (b) Histogram showing probability distribution of equivalent radius of (b1) intermetallic and (b2) pre-existing cavities. ***Intended for color reproduction on the web version.***

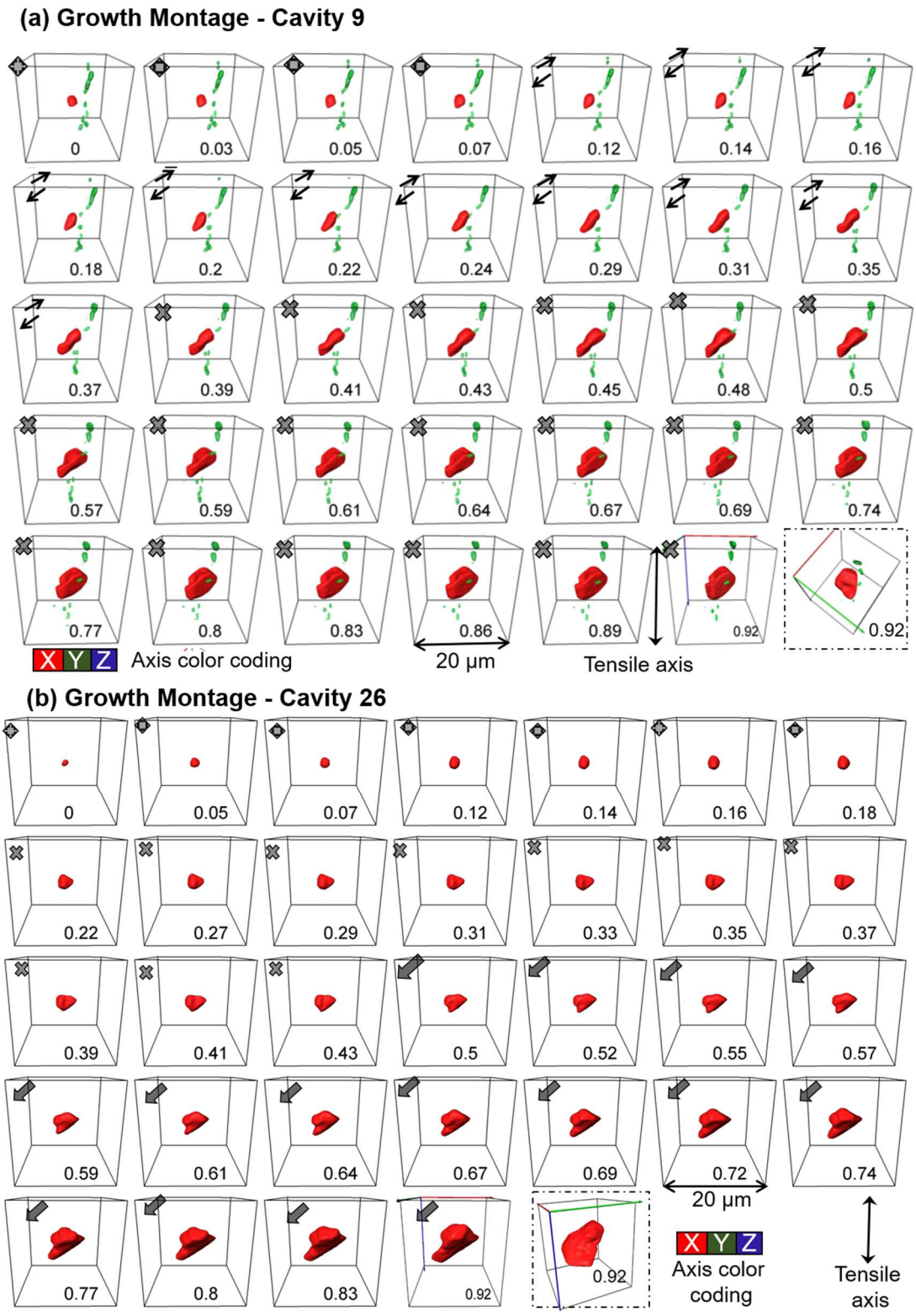

Figure 3 3D rendered volumes showing evolution of the (a) cavity number 9 (b) and cavity number 26 with strain, (marked at the bottom of each box) in sample. Type of evolution has been marked using symbols at top left corner see Figure 6 for reference. A different view of the cavity at the last scan has been also shown (highlighted by a box), for better comprehension of the 3D shape of the cavity (cavities are in red and intermetallics in green). ***Intended for color reproduction on the web version.***

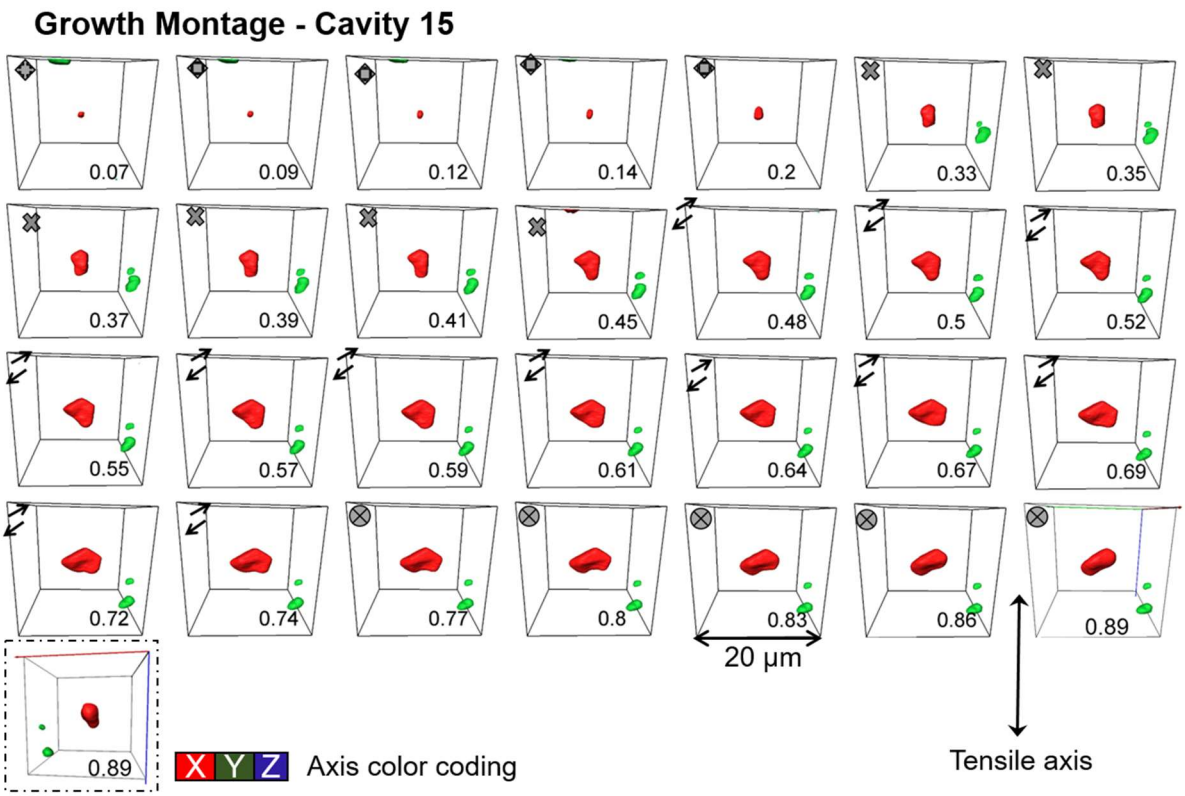

Figure 4 3D rendered volumes showing evolution of the cavity number 15 with strain, (marked at the bottom of each box) in sample. Type of evolution has been marked using symbols at top left corner see Figure 6 for reference. A different view of the cavity at the last scan has been also shown (highlighted by a box), for better comprehension of the 3D shape of the cavity (cavities are in red and intermetallics in green). ***Intended for color reproduction on the web version.***

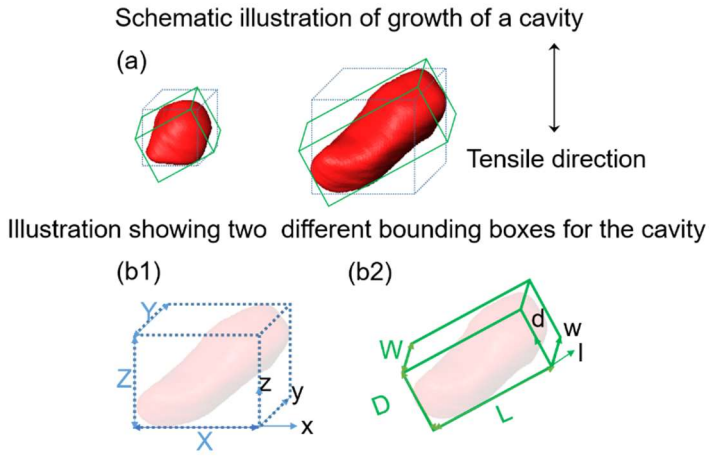

Figure 5 Schematic illustration of (a) growth of a cavity, (b1, b2) two different bounding boxes enclosing the cavity seen in (a). ***Intended for color reproduction on the web version.***

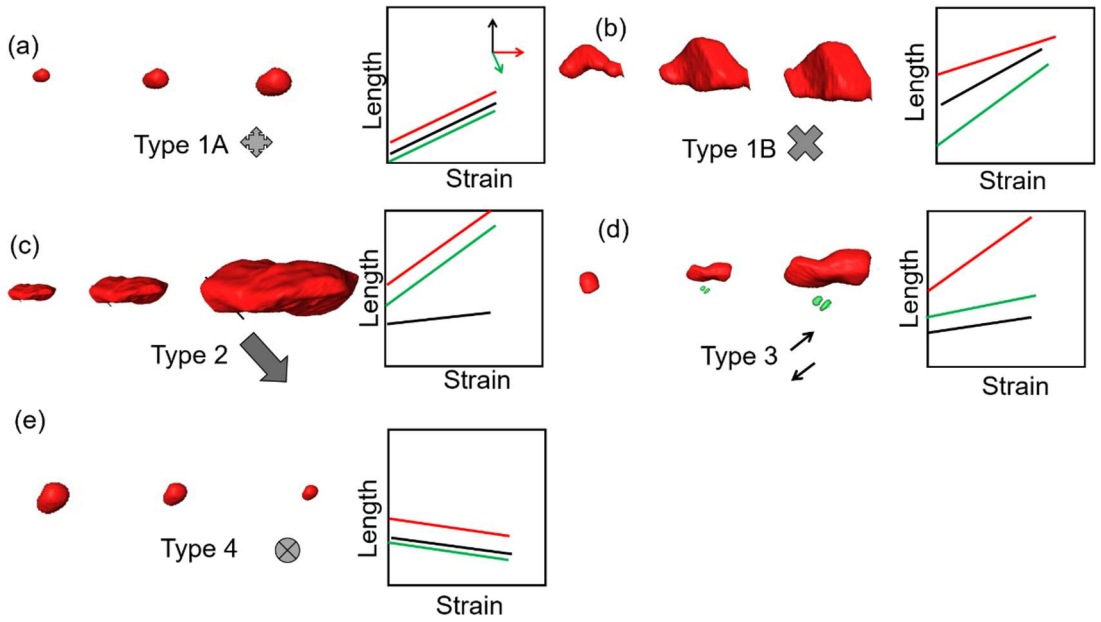

Figure 6 Schematic showing typical examples of evolution of cavity shape for the Evolution Type: (a) Type 1A (b) Type 1B (c) Type 2 (d) Type 3 (e) Type 4 along with assigned symbols. Accompanied by a corresponding plot showing evolution of lengths of bounding box with strain. Orientation of the edges of the bounding box is on the basis of coordinate system shown on top right corner of (a). ***Intended for color reproduction on the web version.***

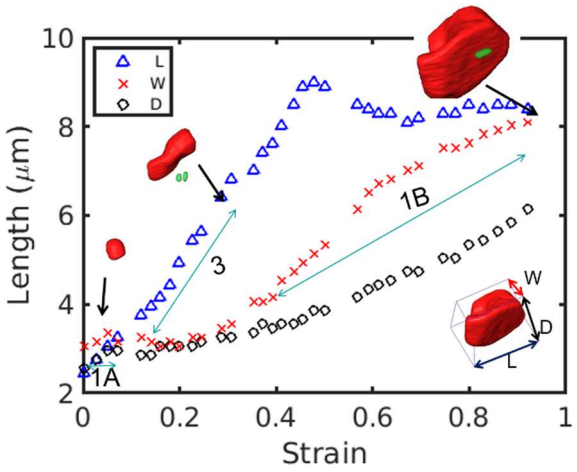

Figure 7 Evolution of L, W and D dimensions (represented by bounding box in right bottom) of cavity number 9 (shown in Figure 3 a) along with strain. The type of evolution (presented in section 3.3) has also been marked along with 3D rendered view of the cavity in different evolution regimes. ***Intended for color reproduction on the web version.***

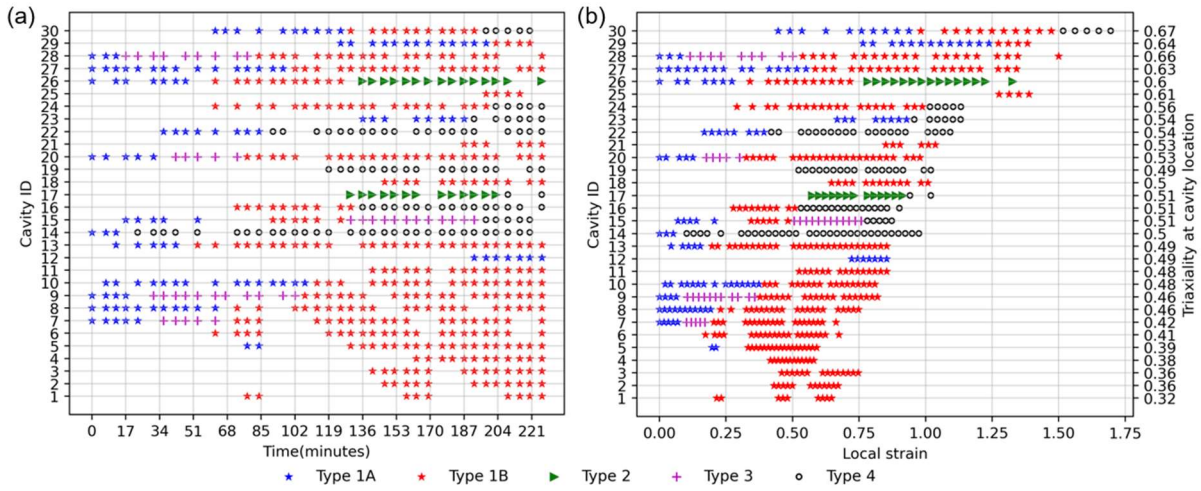

Figure 8 Plot showing pathway of type of evolution, followed by the 30 tracked cavities (a) with time (b) with local strain, the triaxiality associated with each cavity has also been indicated on the y axis to the right. ***Intended for color reproduction on the web version.***

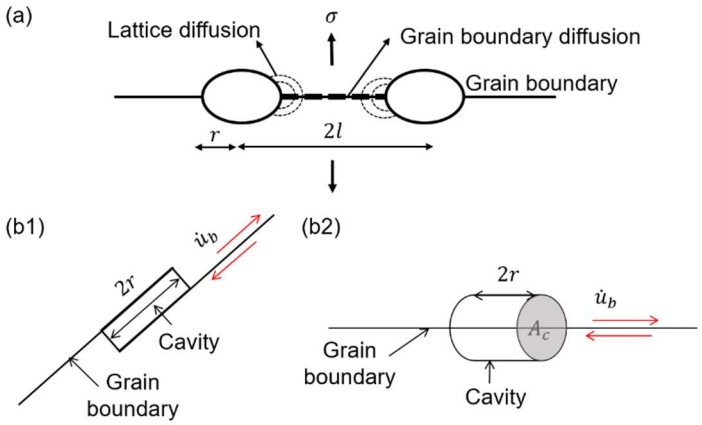

Figure 9 Schematic showing (a) an array of cavities of radius r on a grain boundary, growing via diffusion under the effect of a stress (b) a cavity of length $2r$ lying on a grain boundary sliding at a rate of $\dot{u}_b$ (b1) in 2D [40] *(b2) in 3D (cross section area of cavity transverse to sliding direction is A_c)*

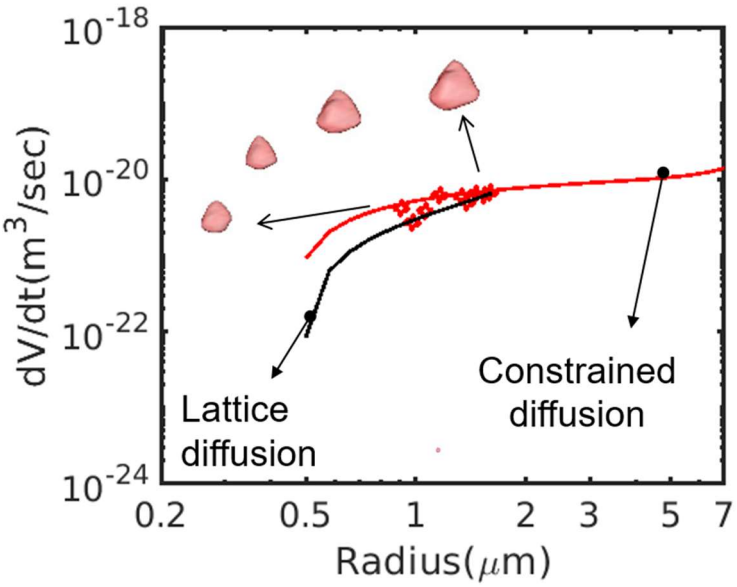

Figure 10 Plots showing volumetric growth rate for a cavity number 8 growing by evolution Type 1A (experimental data shown by red markers). 3D rendered view of cavity during the growth has also been shown for visualization.

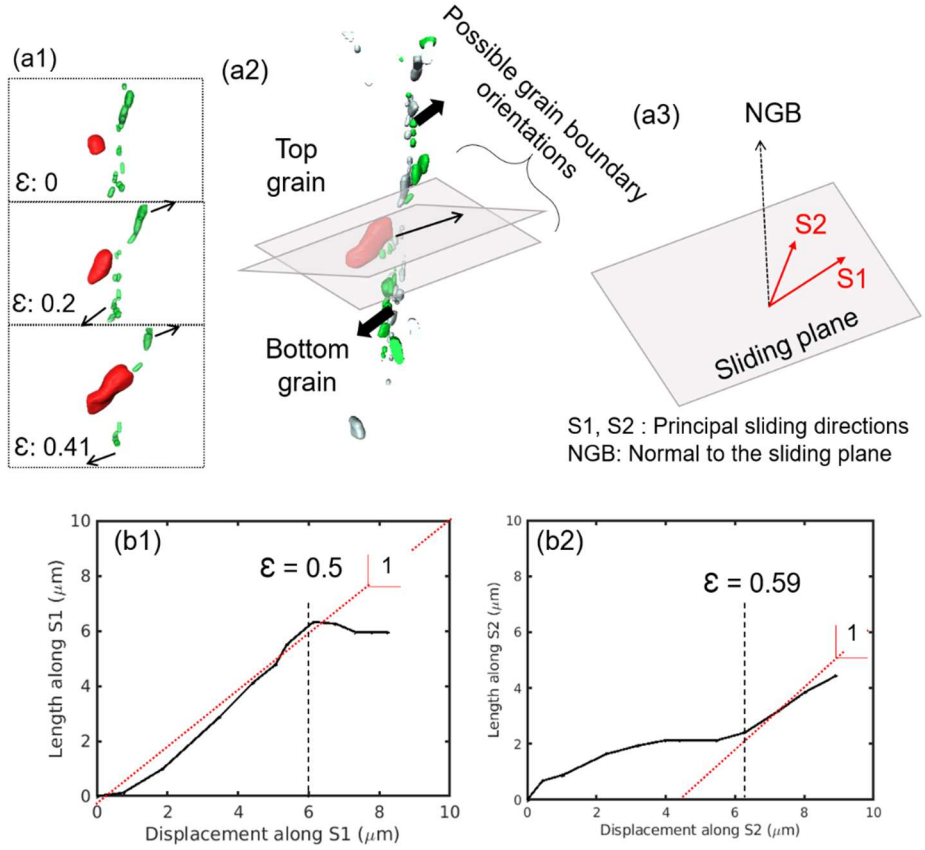

Figure 11 (a1) 3D view of cavity 9 at three strain states. Schematic illustration (a2) showing indication of grain boundary sliding seen through superimposing position of intermetallic in a low (grey) and a high strain state (green) (cavity in red) (a3) of definition of different vectors and directions used in quantifying grain boundary sliding. Plot showing net length of cavity along (b1) S1 direction versus displacement of grain boundary in this direction (b2) S2 direction versus displacement of grain boundary. Red lines are straight lines with slope one, shown to indicate a direct proportionality. ***Intended for color reproduction on the web version.***

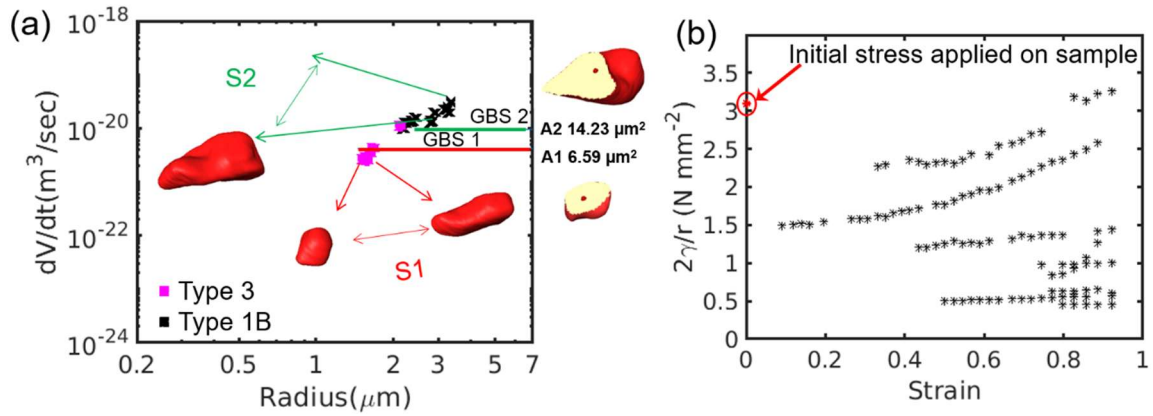

Figure 12 Plot showing (a) volumetric growth rate of cavity number 9, the experimental data is shown by markers. The growth rate by grain boundary sliding (GBS) model corresponding to sliding along S1 shown by green line, (A1 is cross-section transverse to S1) and corresponding to sliding along S2 shown by red line, (A2 is cross-section transverse to S2). 3D rendered view of cavity growing under S1 and S2 sliding have also been shown for reference. (See Figure 3 a for growth montage of this cavity number 9) (b) 2γ/r versus strain for different cavities that evolved by Type 4 mechanism during deformation of the sample. ***Intended for color reproduction on the web version.***